

Supporting information

1 Synthesis

$\text{La}_{0.67}\text{Ca}_{0.33}\text{MnO}_3$ nanoparticles (N-LCMO) were prepared by a polyol sol-gel approach ¹. 4.6 mmol of lanthanum (II) nitrate exahydrate (Fluka analytical, > 99 %), 2.3 mmol of calcium (II) nitrate tetrahydrate (Sigma Aldrich, 99 %) and 6.9 mmol of manganese (II) nitrate tetrahydrate (Sigma Aldrich, > 97 %) were mixed in an equal weight of distilled water in a 250 ml becker. Ethylene glycol (EG, Sigma Aldrich, 99.8 %) was added (1.5 times the volume of water) and the solution was kept at 80°C on a hotplate for 20 minutes, under magnetic stirring. Then, the solution was kept at 150°C until the gel was formed, and finally, the temperature was increased to 300°C to induce the self-combustion. The obtained powder was finally calcinated at 550°C for 2 hours.

CoFe_2O_4 nanoparticles (N-CFO) were prepared by polyol process ²⁻⁴. 2 mmol of iron (III) nitrate nonahydrate (Sigma Aldrich, > 98 %), 1 mmol of cobalt (II) nitrate exahydrate (Sigma Aldrich, 98 %) and 1ml of distilled water were added to 100 ml of tri-ethylene glycol (TEG, Sigma Aldrich, 99 %) in a round bottom tree-neck flask. The solution was kept under mechanical agitation and heated to the boiling point. The system was kept under reflux for 2h; then it was cooled to room temperature. With the addition of acetone, the precipitation of a black powder was induced. The product was washed with acetone and separated via centrifuge; this procedure was repeated three times, finally, the powder was dried in an oven at 60°C overnight.

2 Morpho-structural analysis

XRD patterns of samples N-LCMO and N-CFO (**figure S2**) show reflections of $\text{La}_{0.67}\text{Ca}_{0.33}\text{MnO}_3$ perovskite (PDF card 01-089-6933) and CoFe_2O_4 cubic spinel oxide (PDF card 01-079-1744) structures, respectively. No reflections of any other phases are detected. Both N-MIX and NC XRD patterns (**figure S2**) presents only the main reflections of both LCMO and CFO crystalline structures.

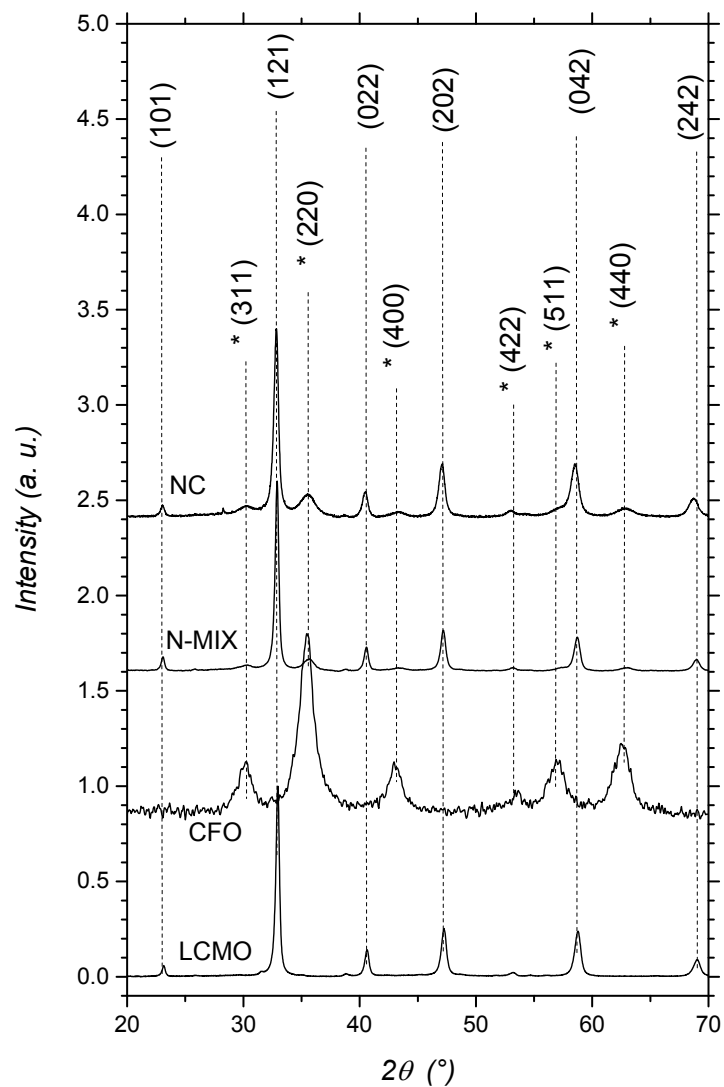


Figure S1. XRD patterns of pure N-LCMO and N-CFO and composites N-MIX and NC. All reflections perfectly match with those of $\text{La}_{0.67}\text{Ca}_{0.33}\text{MnO}_3$ (ICDD card 00-049-0416) and CoFe_2O_4 (ICDD card 00-079-1744) phases (marked as *).

TEM images of all samples are reported in figure S2 and S3, to show the detailed structure of both the pure phases and the composites samples.

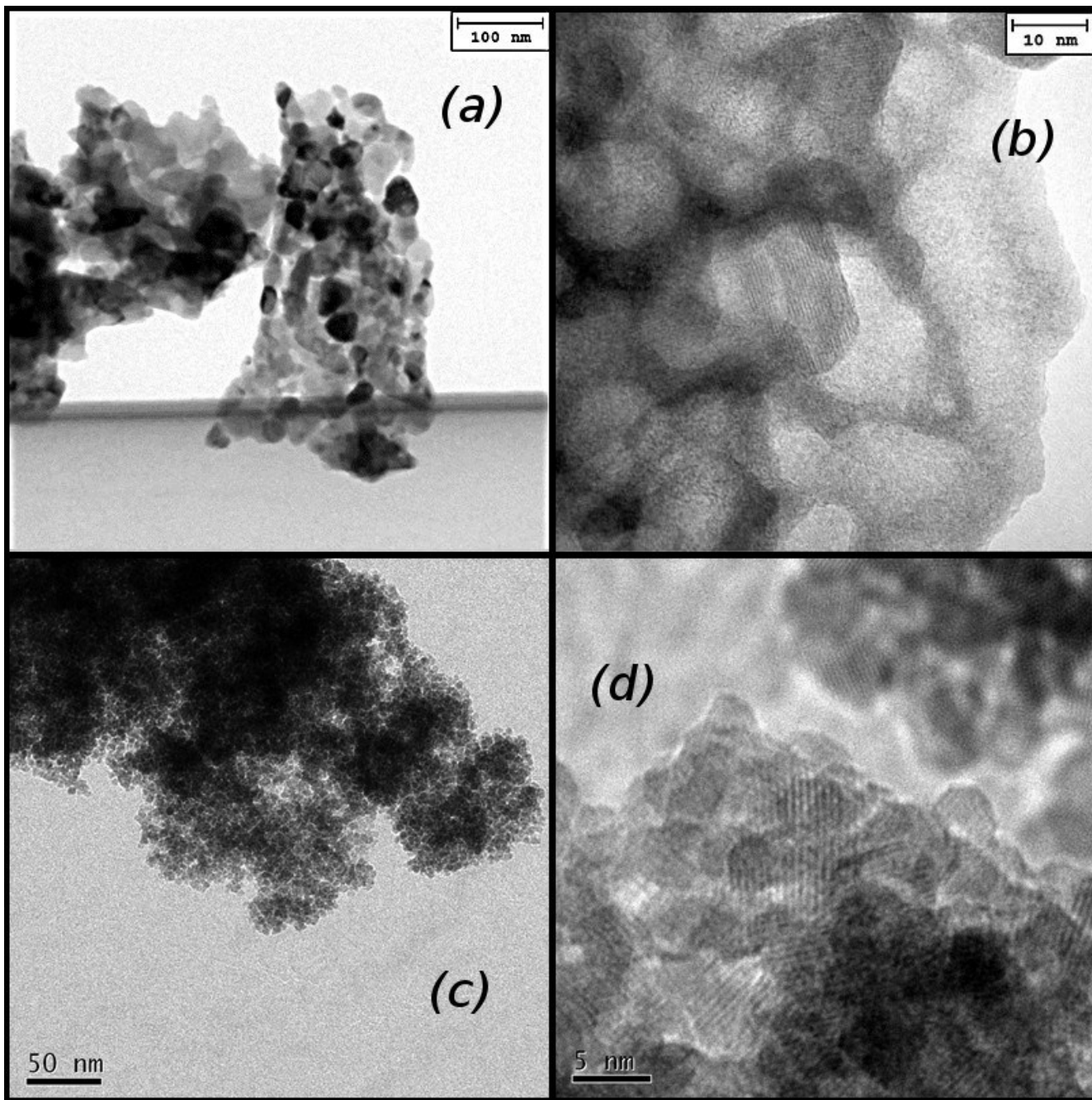


Figure S2: TEM images of sample N-LCMO (a and b), N-CFO (c and d) at different magnifications.

2.1 Calcination process

A calcination process is employed in order to produce the complete crystallization of the manganite phase. After several attempts at different temperature, the optimal condition has been reached at 550 °C (**figure S1**), reaching the complete crystallization as the lowest possible temperature in order to retains the smallest particles size.

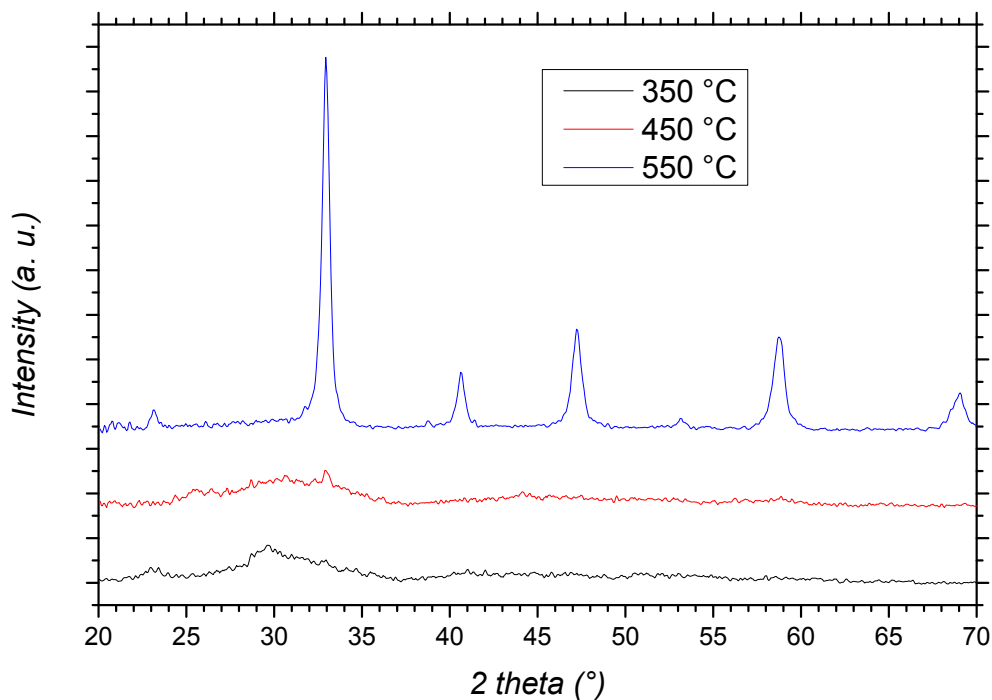


Figure S3. XRD pattern of $\text{La}_{0.67}\text{Ca}_{0.33}\text{MnO}_3$ phase calcinated at several temperatures.

2.2 Cobalt doping effect

In order to clarify the eventual diffusion of cobalt, from CFO to LCMO phase in NC sample, a comparison of the $\text{La}_{0.67}\text{Ca}_{0.33}\text{MnO}_3$ (ICSD 155408) and $\text{La}_{0.67}\text{Ca}_{0.33}\text{Mn}_{0.9}\text{Co}_{0.1}\text{O}_3$ (ICSD 165817) phases with the experimental pattern of the sample has been produced. As shown in the pattern magnification in **figure S1**, the presence of Co as dopant should produce a quite clear shift in the experimental data. If the Rietveld refinement is conducted considering the two LCMO phases, the best fit corresponds to 1% in weight of the cobalt-doped phase, under what it can be considered the experimental error on this measurement (estimated around 5%). Furthermore, if the fitting is forced using only the Co doped phase, but leaving the Co and Mn contents as free parameter, the best fit evaluates the Mn content as 0.9999 and the Co as 0.0001, strongly supporting its absence.

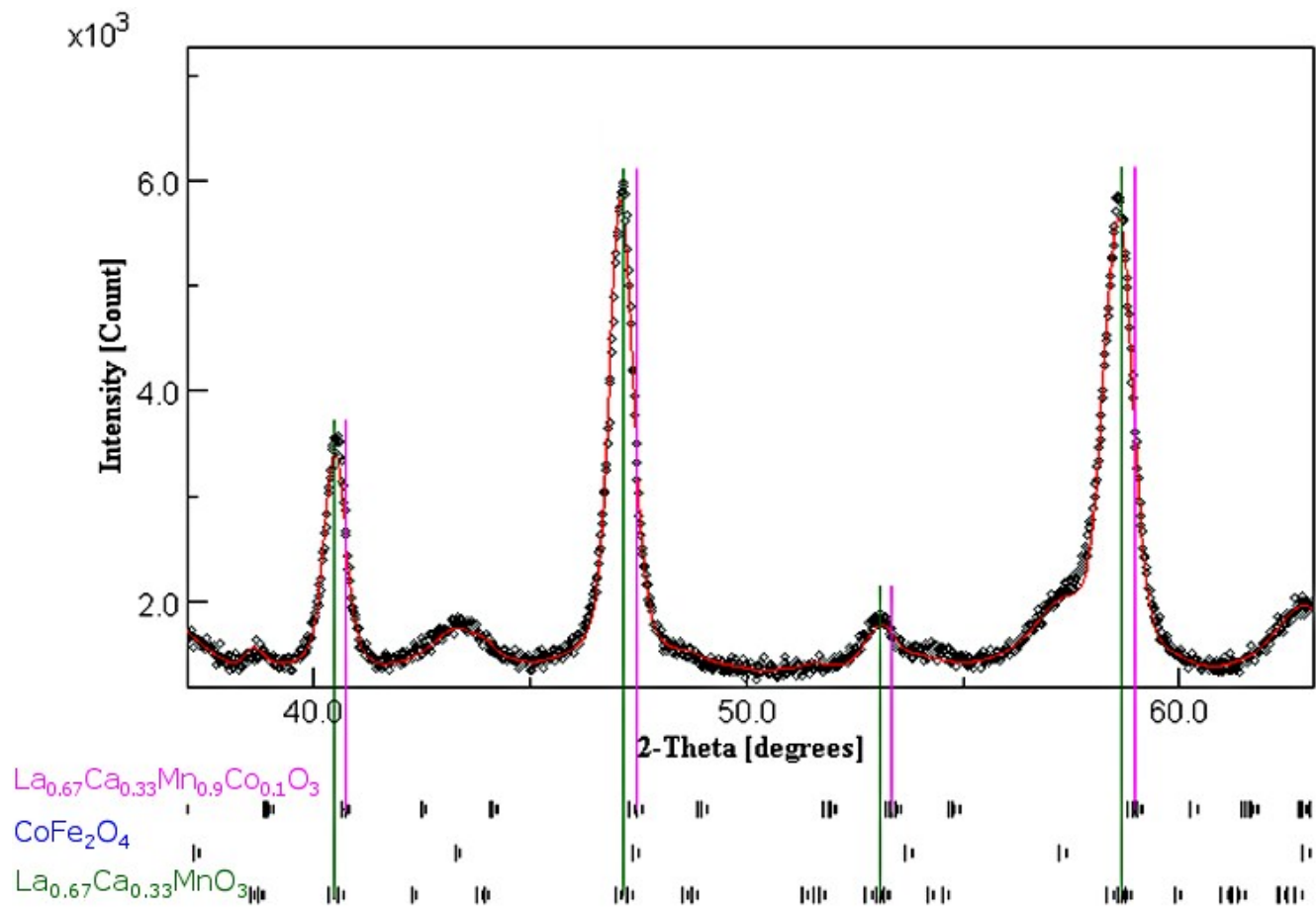


Figure S4. Magnification of XRD pattern of NC sample in the range 35-65° (2-Theta).

3 Detailed comparison of pure phases and composites magnetic curves

3.1 Simulated ZFC-FC curves for N-MIX sample

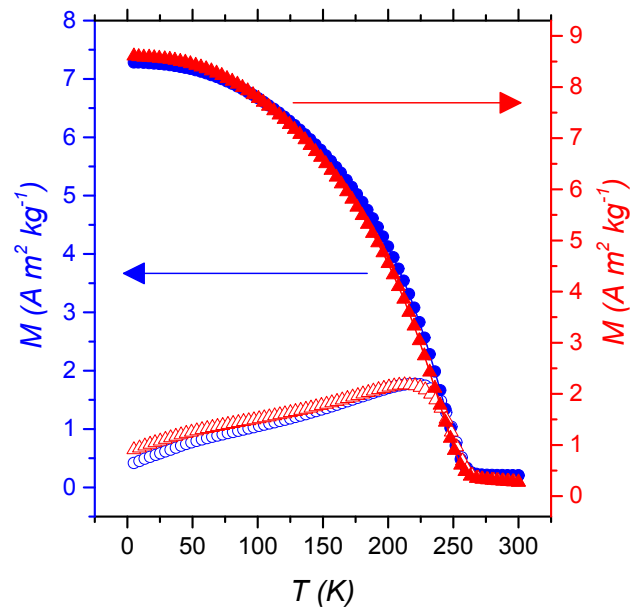


Figure S5. The experimental ZFC-FC curve (empty and full blue circles, respectively) and the artificial one (empty and full red triangles, respectively) are shown. The two curves exhibit similar trends, with no clear evidence of the CFO contribution.

3.2 TRM and derivative curves analysis

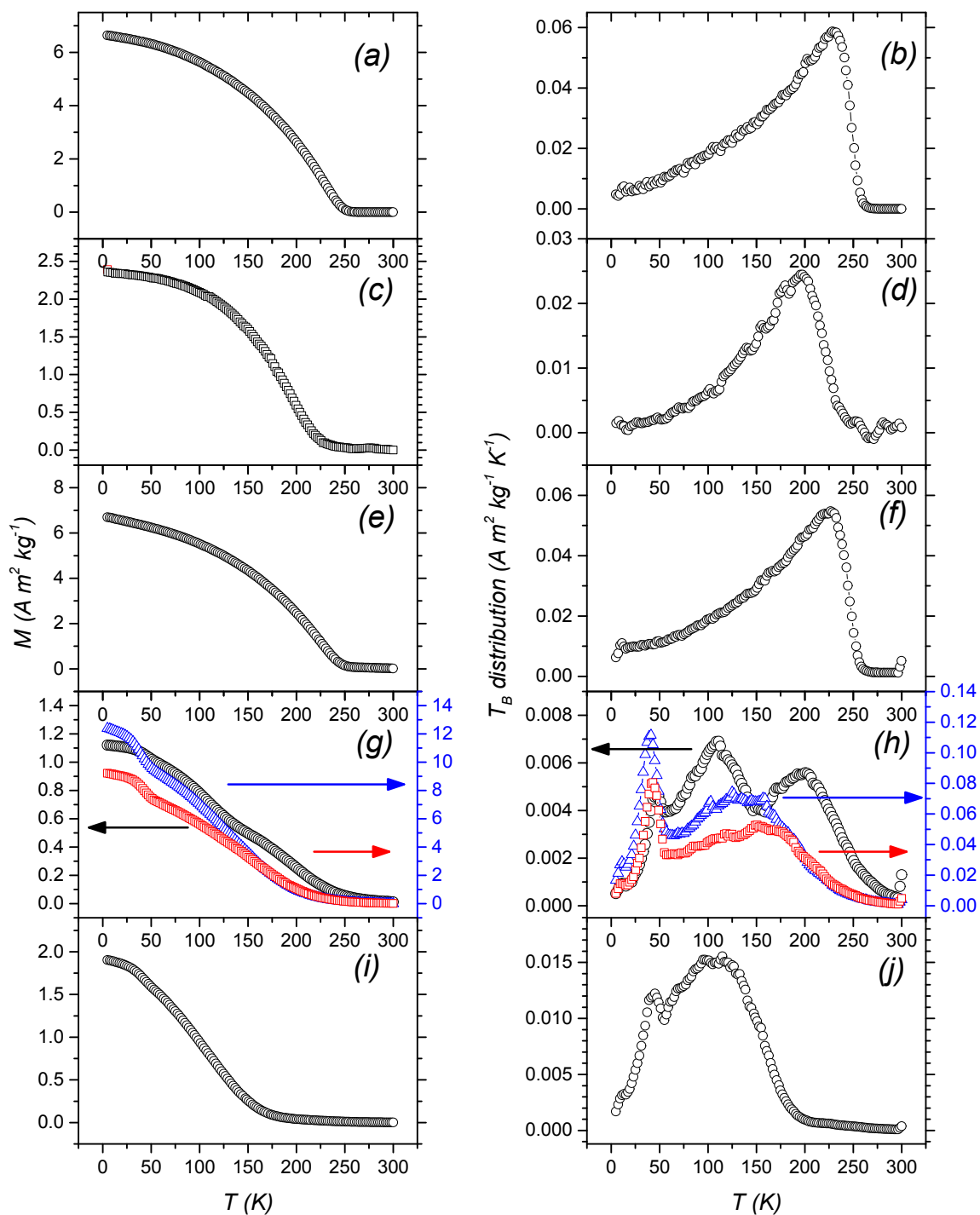


Figure S6. The TRM curves measured after a field cooling of 2.5 mT and their derivatives are shown for N-LCMO (a and b), N-CFO (c and d), N-MIX (e and f), NC (g and h) and NC2 (i and j). For NC, the curves measured after a field cooling of 2.5 mT, 50 mT and 100 mT are represented as black circles, red squares, and blue triangles, respectively.

For an ensemble of non-interacting nanoparticles, information about the effective magnetic anisotropy energy distribution $f(T)$ can be obtained by the TRM derivative curve ⁵:

$$f(t) \propto -\frac{dM_{TRM}}{dT} \quad (4)$$

These two quantities are proportional, thus, a given temperature T' , the thermal energy kT' allows a fraction of particles to overcome their anisotropy energy barrier and to act as superparamagnet. At that temperature, the ratio between the fraction of unblocked (P_{SPM}) and that of blocked (P_B) particles can be defined as ⁶:

$$R(T') = \frac{P_{SPM}}{P_B} = \frac{\int_{T'}^{T_{max}} f(T)dT}{\int_{T_{min}}^{T'} f(T)dT} \quad (5)$$

where T_{min} and T_{max} represent the minimum and maximum temperatures covered in the range of measurement. According to the relation (4) and (5), the temperature corresponding to a value $R = 1$ is identified as that in which the integral of the TRM derivative curve reaches 50% of its maximum value; such temperature is usually considered as the average blocking temperature T_B of the sample ^{6,7}. However, this definition does not consider the number of particles involved in the SPM state, owning bigger particles larger magnetization contribution on the curve, in addition, as in composite samples, more than one distribution can be present, thus the evaluation of the respective average blocking temperature cannot be solved through the integral method. An alternative is to define T_B as the temperature corresponding to the peaks of the derivative curve ^{8,9}, assuming that the particles size distribution is symmetric. It is worth to mention that this evaluation can introduce a difference smaller than 10 % with respect the other definition ⁶.

$d(TRM)/dT$ of NC sample (**figure S6h**) shows a peak at ≈ 190 K (TRM curve measured after field cooling of 2.5 mT), perfectly compatible with the SPM behavior of pure CFO (**figure S6d**). Furthermore, two signals, centered at ≈ 111 K and ≈ 50 K are identified. In order to better analyze the nature of these two signals, the TRM and derivative curves have been measured after field cooling at 50 and 100 mT (**figure S6g**). The peak at highest temperature shows a field dependent behavior, in agreement with the SPM blocking of CFO phase. On the other hand, the peak at ≈ 111 K does not show such field dependence, confirming that it can be related to the drop of the magnetization due to the LCMO FM / PM transition, which occurs at a temperature lower than expected (≈ 260 K). Again, this interpretation can be confirmed by the TRM of NC2 sample reported in **figure**

S6i and **j**, where a $T_C \approx 200$ K can be estimated. Such T_C shift could be ascribed to cobalt or iron doping in LCMO structure, owing to the thermal treatment on the composite. Nevertheless, carefully analyzing the XRD pattern, no trace of such cobalt inclusion has been evidenced (**figure S4**). On the nanoscale, a disordered magnetic structure arises at particles surface due to broken lattice symmetry and possible defects. Such defects induce larger Mn-O distance and a corresponding smaller Mn-O-Mn angle, inducing an effect on the local T_C temperature. Reducing particles size, the surface to volume ratio increases and the surface disorder has a strong influence on the T_C of the whole particle, in particular under 40 nm, as experimentally observed by Markovic et al.¹⁰. Conflicting experimental results have been reported in literature for particle size dependence of manganites T_C , probably mainly due to slightly different oxygen content and preparation procedure, which has a strong influence on particles surface. Anyway, Montecarlo simulations have shown that the reduced ionic coordination at particles surface lowers the T_C for nanoparticles¹¹, as confirmed by a systematic study on the effect of particles size on $\text{La}_{0.6}\text{Pb}_{0.4}\text{MnO}_3$ by Zhang et al.¹². The monodomain critical radius for manganites has been predicted around 40 nm¹³ and a SPM blocking or spin-glass like freezing has been suggested by several authors¹⁴⁻¹⁶. Anyway Markovich et al.¹⁰ have found similar T_C size dependence, observing that the ZFC curve peak has an AC frequency dependence, typical of interacting SPM particles, only for size around 10 nm, enforcing the hypothesis of a simple phase transition origin of the peak.

Finally, in all $d(\text{TRM})/dT$ curves of NC, a small peak appears at ≈ 50 K. Several authors have claimed to observe a spin-glass-like behavior in LCMO around ≈ 40 -50 K¹⁷⁻¹⁹, but in most of the cases this can be assimilated to the paramagnetic-ferrimagnetic (PM-FiM) transition of Mn_3O_4 impurities ($T_N = 43$ K)^{20,21}. This can give a significant magnetic contribution even with an amount that is smaller than the XRD detection limit²². A second possible origin for such peak can be the freezing of a disordered surface shell on a ordered FM core, as reported by Zhu et al. for LSMO particles under 50 nm²³. However, no field dependence of this peak is observed by measuring ZFC-FC-TRM in different fields, instead, an increment of the magnetization compatible with a small fraction of impurities is evident.

3.3 IRM, DCD and ΔM -plots

For a more complete analysis of the two composites, a comparison with the pure LCMO and CFO phases has been carried out. For the sake of clarity, the detailed IRM and DCD curves, with the respective derivatives are measured for each sample and shown in **figure S7**, while the obtained ΔM plots are compared in **figure S8**.

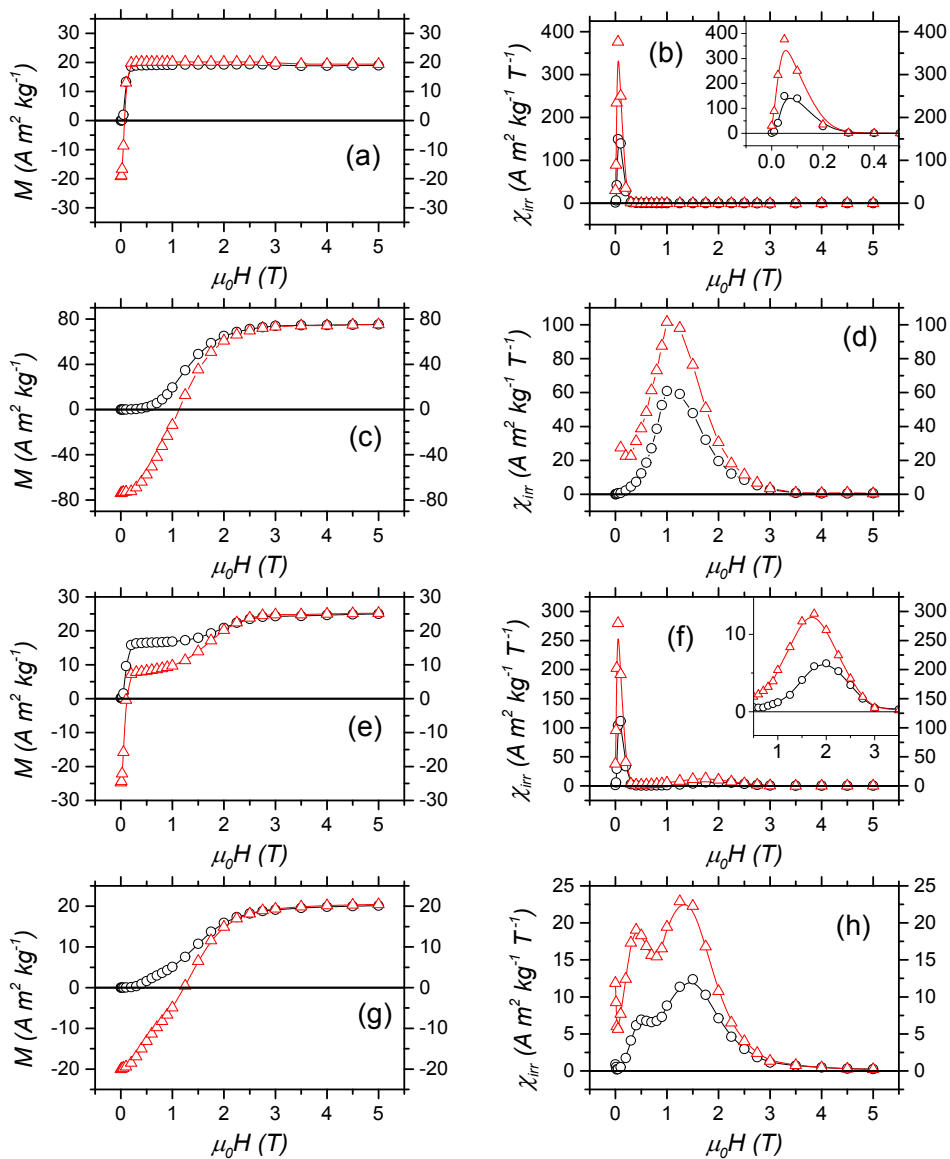


Figure S7. IRM (black circles) and DCD (red triangles) curves of samples N-LCMO (a), N-CFO (c), N-MIX (e) and NC (g). The corresponding derivatives curves $dIRM/d\mu_0 H$ (black circles) and $dDCD/d\mu_0 H$ (red triangles) are reported in panels b, d, f and h for samples N-LCMO, N-CFO, N-MIX and NC, respectively, with a data magnification reported in insets.

ΔM -plots clarify the interparticle interactions picture for both N-MIX and NC samples. For a system with uniaxial anisotropy and without interparticles interactions, the same energy barrier is calculated from IRM and DCD curves, as in Wohlfarth relation ²⁴:

$$M_{DCD}(H) = 1 - 2M_{IRM} \quad (2)$$

Kelly et al. rewrote this expression as ²⁵:

$$\Delta M = M_{DCD}(H) - 1 + 2M_{IRM} \quad (3)$$

Negative deviations in ΔM are usually taken as indicative of the presence of interactions that stabilize the demagnetized state (i.e., dipole-dipole interactions). Positive values are attributed to interactions promoting the magnetized state (i.e., exchange interactions).

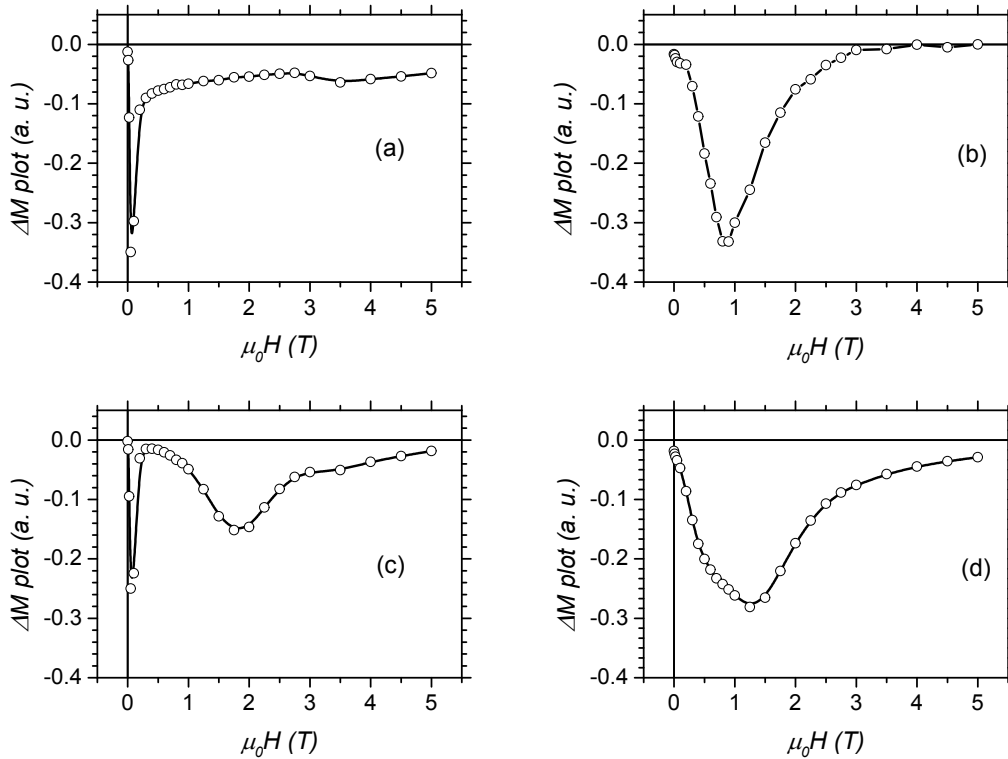


Figure S8. ΔM plots of samples N-LCMO (a), N-CFO (b), N-MIX1 (c) and NC (d).

4 Influence of CFO content

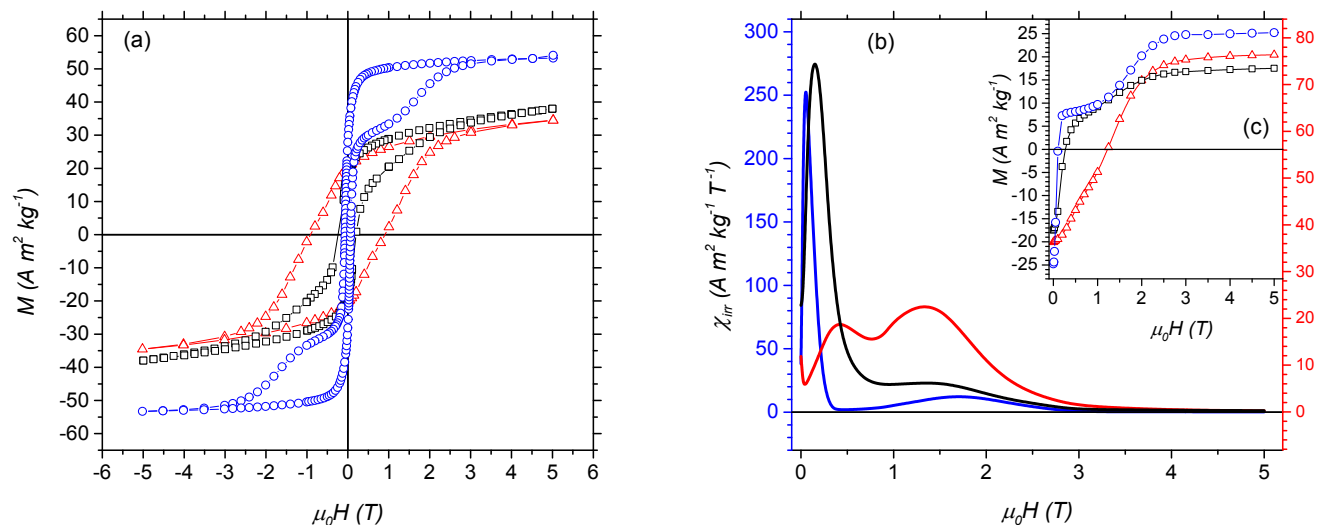


Figure S9. (a) M Vs H curves of NC1 (red triangles), NC2 (black squares) and N-MIX (blue circles). (b) Switching field distribution curves for sample NC1 (red), NC2 (black) and N-MIX (blue), as obtained from the first order derivative of the DCD curves, which are reported in the inset (c). All curves were measured at a temperature of 5 K.

Figure S9a reports the M - H curves for NC1 and NC2 nanocomposites along with N-MIX sample. The two samples show comparable saturation magnetization, higher in NC2 (≈ 45 vs $40 \text{ A m}^2 \text{ kg}^{-1}$ extrapolated at high field using the law of approaching saturation²⁶), in addition, both present similar remanence magnetization, within the experimental error. However, NC1 shows a stronger hysteretic behavior, with a much higher coercive field ($\approx 0.91 \text{ T}$ vs 0.20 T) which can be linked to the higher CFO content (≈ 40 vs 5%). At a first sight, the NC2 curve reveals the possible presence of two magnetic phases, while this is much less visible with comparison to the curve of N-MIX, reported for comparison. This hypothesis is confirmed by analyzing the SFD distributions (figure S9b). The two peaks in NC2 curve are closer when compared to that in sample N-MIX, underlining the coupling between the two phases. However, such coupling is clearly less intense compared to that of NC1. This coupling effect, matched with the reduced amount of CFO phase, improved the magnetoresistance of the nanocomposites. Indeed the analysis of R Vs H curve for sample NC2 revealed a magnetoresistance effect of the same order of magnitude of sample N-MIX (figure 4). In addition, the R - H loops measured at different temperatures, presented the inversion of the $\mu_0 H_c^{MR}$ values in a similar way to N-MIX. A conventional curve is measured at 100 K , while increasing the temperature, the maximum reduce up to inverse

at 200 K (figure S10d), demonstrating that it is possible to tune both the magnetic coupling and the magneto-transport properties optimizing the morphology of the NC composites.

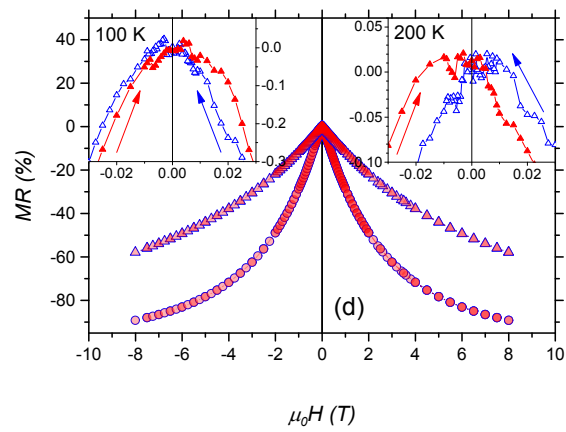
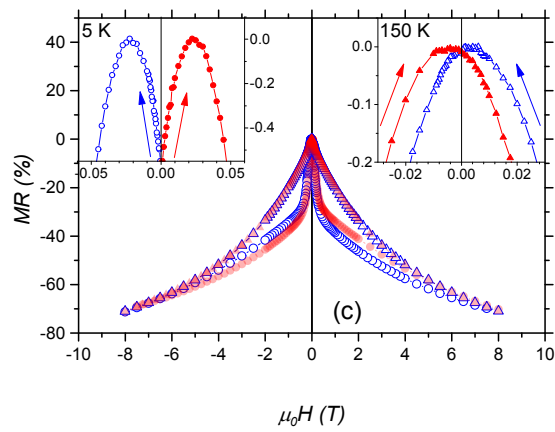
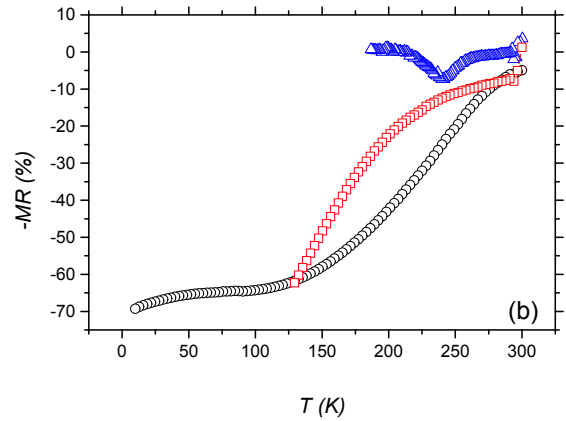
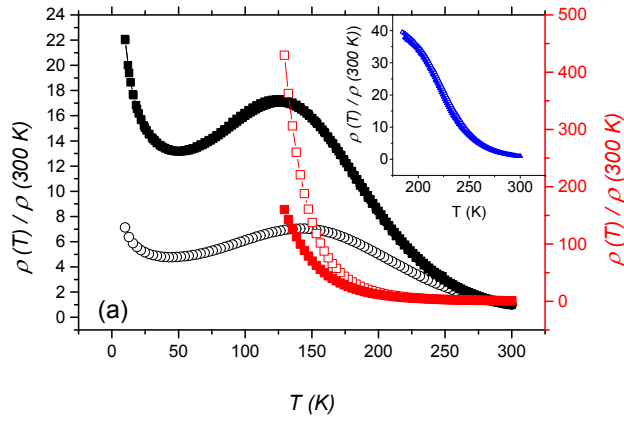


Figure S10: The temperature dependence of the resistance is reported for sample N-MIX (black circles), NC (blue triangles) and NC2 (red squares) in panel (a) without (empty symbols) and with a 5 T magnetic field applied (full symbols). It is important to note that for sample NC the two curves are almost perfectly superimposed. Panel (b) reports the temperature dependence of the magnetoresistance for N-MIX (black circles), NC (blue triangles) and NC2 (red squares). The magneto-resistance for N-MIX, measured at 5 K (circles) and 150 K (triangles) are reported in panel (c), while for sample NC2 the curves measured at 100 K (circles) and 200 K (triangles) are reported in panel (d). Blue empty symbols are used for the branch measured sweeping the field from +8 to -8 T, and red full symbols for the one measured from -8 to +8 T. A magnification at low field is reported in the respective insets, with arrows indicating the direction of field sweeping. References

- 1 T. Sarkar, a K. Raychaudhuri, a K. Bera and S. M. Yusuf, *New J. Phys.*, 2010, **12**, 123026.
- 2 F. Fiévet and R. Brayner, in *Nanomaterials: A Danger or a Promise?*, eds. R. Brayner, F. Fiévet and T. Coradin, Springer London, 2013, pp. 1–25.
- 3 S. Ammar, A. Helfen and N. Jouini, *J. Mater. Chem.*, 2001, 186–192.
- 4 S. Chkoundali, S. Ammar, N. Jouini, F. Fiévet, P. Molinié, M. Danot, F. Villain and J.-M. Grenèche, *J. Phys. Condens. Matter*, 2004, **16**, 4357–4372.
- 5 D. Peddis, D. Rinaldi, G. Ennas, A. Scano, E. Agostinelli and D. Fiorani, *Phys. Chem. Chem. Phys.*, 2012, **14**, 3162–9.
- 6 A. J. Rondinone, C. Liu and Z. J. Zhang, *J. Phys. Chem. B*, 2001, **105**, 7967–7971.
- 7 C. Cannas, A. Musinu, G. Piccaluga, D. Fiorani, D. Peddis, H. K. Rasmussen and S. Mørup, *J. Chem. Phys.*, 2006, **125**, 164714 1–11.
- 8 B. N. Pianciola, E. Lima, H. E. Troiani, L. C. C. M. Nagamine, R. Cohen and R. D. Zysler, *J. Magn. Magn. Mater.*, 2015, **377**, 44–51.
- 9 M. Sasaki, P. Jönsson, H. Takayama and H. Mamiya, *Phys. Rev. B*, 2005, **71**, 1–9.
- 10 D. Markovic, V. Kusigerski, M. Tadic, J. Blanusa, Z. Jaglicic, N. Cvjeticanin and V. Spasojevic, *J. Alloys Compd.*, 2010, **494**, 52–57.

- 11 E. Restrepo-Parra, G. Orozco-Hernández and J. C. Riaño-Rojas, *J. Magn. Magn. Mater.*, 2013, **344**, 44–48.
- 12 T. Zhang, G. Li, T. Qian, J. F. Qu, X. Q. Xiang and X. G. Li, *J. Appl. Phys.*, 2006, **100**, 094324.
- 13 V. M. Andrade, R. J. Caraballo-Vivas, T. Costas-Soares, S. S. Pedro, D. L. Rocco, M. S. Reis, A. P. C. Campos and A. a. Coelho, *J. Solid State Chem.*, 2014, **219**, 87–92.
- 14 V. Spasojevic, A. Mrakovic, M. Perovic, V. Kusigerski and J. Blanusa, *J. Nanoparticle Res.*, 2010, **13**, 763–771.
- 15 A. Rostamnejadi, H. Salamati, P. Kameli and H. Ahmadvand, *J. Magn. Magn. Mater.*, 2009, **321**, 3126–3131.
- 16 S. Xi, W. Lu and Y. Sun, *J. Appl. Phys.*, 2012, **111**, 063922.
- 17 P. Dey, T. K. Nath, P. K. Manna and S. M. Yusuf, *J. Appl. Phys.*, 2008, **104**, 103907.
- 18 T. Ji, J. Fang, V. Golob, J. Tang and C. J. O'Connor, *J. Appl. Phys.*, 2002, **92**, 6833.
- 19 S. B. Xi, W. J. Lu, H. Y. Wu, P. Tong and Y. P. Sun, *J. Appl. Phys.*, 2012, **112**, 123903.
- 20 J. Du, Y. Gao, L. Chai, G. Zou, Y. Li and Y. Qian, *Nanotechnology*, 2006, **17**, 4923–4928.
- 21 R. Bussamara, W. W. M. Melo, J. D. Scholten, P. Migowski, G. Marin, M. J. M. Zapata, G. Machado, S. R. Teixeira, M. a Novak and J. Dupont, *Dalton Trans.*, 2013, **42**, 14473–9.
- 22 D. Choudhury, S. Mukherjee, P. Mandal, A. Sundaresan, U. V. Waghmare, S. Bhattacharjee, R. Mathieu, P. Lazor, O. Eriksson, B. Sanyal, P. Nordblad, A. Sharma, S. V. Bhat, O. Karis and D. D. Sarma, *Phys. Rev. B*, 2011, **84**, 125124.
- 23 T. Zhu, B. G. Shen, J. R. Sun, H. W. Zhao and W. S. Zhan, *Appl. Phys. Lett.*, 2001, **78**, 3863.
- 24 E. P. Wohlfarth, *J. Appl. Phys.*, 1958, **29**, 595–596.
- 25 K. O'Grady and R. W. Chantrell, 1992.
- 26 H. Zhang, D. Zeng and Z. Liu, *J. Magn. Magn. Mater.*, 2010, **322**, 2375–2380.

